-RESEARCH PAPER-

International Journal of Mining and Geo-Engineering

IJMGE

IJMGE 55-2 (2021) 171-181

DOI: 10.22059/IJMGE.2021.309744.594863

Geochemical descriptions of iron-oxide targets by Prediction-Area plot and Concentration-Number fractal model in Esfordi, Iran

Fardin Ahmadi [a, *], Hamid Aghajani [a], Maysam Abedi [b]

[a] *Faculty of Mining, Petroleum and Geophysics, Shahrood University of Technology, Shahrood, Iran*

[b] *School of Mining Engineering, College of Engineering, University of Tehran, Tehran, Iran*

Article History:

Received: 09 September 2020,

Revised: 01 January 2021,

Accepted: 15 January 2021.

ABSTRACT

This study serves the purpose of generating a geochemical Fe-bearing potential map. Stream sediment geochemical survey was employed by collecting 843 samples for analyzing 19 elements and oxides. Taking preprocessing of data (e.g. outlier correction and data normalization) into consideration, a Concentration - Number (C-N) fractal model was used to separate different geochemical populations of Fe_2O_3, TiO_2, *V*, and the main multi-element factor in close spatial association with the Fe targeting. A prediction-area(P-A) plot was drawn for each variable to determine the weight of each geochemical indicator. Results indicate that the main geochemical factor with an ore prediction rate of 73%, has occupied 27% of the Esfordi area as favorable zones for further mining prospectivity. The Esfordias a favorable Fe-bearing zone is of special interest in the NE of the Bafq mining district that hosts important "Kiruna-type" Magnetite-Apatite deposits. In addition, a synthesized indicators map was prepared by implementing a data-driven multi-class index overlay in a similar fashion to the previous version of the method, upon which geochemical potential zones were mostly in the NE part of the Esfordi, intimately linked with intense fault density map. The significance of this study lies in localizing the most geochemical favorable zones through simultaneous consideration of the C-N and P-A plots accompanied by the incorporation of known active mines and prospects to determine indicator weight. Of note is that the Mineral Potential Mapping(MPM) has higher efficiency over each geochemical indicator with an ore prediction rate of 78% and area occupation of 22%.

Keywords: *Esfordi, Stream sediment, C-N fractal model, P-A plot, Data-driven index overlay*

1. Introduction

Iron targets in Iran formed during several metallogenic phases in Neoproterozoic-early Cambrian, late Cambrian-Early Ordovician, late Paleozoic, Mesozoic, and Cenozoic. Note that the largest occurrences were deposited during the Neoproterozoic-early Cambrian (mainly Kiruna-type deposits) and Cenozoic (skarn) [1-8]. The iron oxide-apatite deposits are often hosted by lower Cambrian hydrothermally altered and alkali-metasomatized volcano-sedimentary rocks known as the Saghandformation, formed during a major late Precambrian rifting event[4; 7-12]The international iron ore market has recently attracted much attention due to strong demand from the steel industries. Mining capacities are extended worldwide, and the Central Iranian Bafq iron ore district is an active area of mining prospectivity. Many iron occurrences exist in the central Iranian structural zone, especially in the Bafq district. The Esfordi prospect zone locates in this region by encompassing several iron mines, e.g. Chadormalu, Choghart, Seh-Chahoon, Mishdowan, and Zaghia [13-14]. The genesis of the magnetite-apatite deposits of the Bafq district is yet controversial among geoscientists, similar to their world counterparts. It's worth pointing out that several different tentative genetical models from carbonatitic to iron ore magma (intrusion or volcanic) and metasomatic replacement were proposed [2; 4; 9; 15-16].

A geochemical anomaly separation is a useful tool for geochemical exploration. The anomalous threshold, which is the most useful criteria for cross-examination of information with numerical data from different sources, commonly used in geochemistry studies [17-19]. Predictive modeling of mineral prospectivity using Geographic Information System (GIS) is a valid and progressively more accepted tool for delineating reproducible mineral exploration targets. Anomalous geochemical zones could be defined at values greater than a given threshold. Various statistical methods have attracted the attention of scholars based on a certain assumption about the underlying statistical distribution of the geochemical variables to determine anomaly threshold values for separating geochemical populations in association with sought ore target [20-22]. Recognition and separation of anomalous zones from background area integral parts of any geochemical exploration investigations [23-24].While traditional methods based on classical statistics are suffering from lots of limitations and pitfalls. There is clear information in the data that is not being captured by running conventional approaches. A possible scenario to strive is utilizing the fractal methods [25]

Various versions of fractal/multifractal modeling, established by Mandelbrot (1983) [25], have been proposed in geochemical data analysis. There have been several studies dedicated to the use of these versions that are Number-Size (N-S) by Mandelbrot (1983), Concentration-Area (C-A) by Cheng et al. (1994) [26], Concentration-Distance (C-D) by Li et al. (2003) [24] Concentration-Volume (C-V) by Afzal et al. (2011) [27] and Concentration-Number (C-N) by Hassanpour and Afzal (2013) [28]. One of the main characteristics of the fractal models over the statistical methods is the consideration of the spatial status of data samples [26, 29-31], reflecting the geological, geochemical, and mineralogical sequences of a region [23-24]. Based on

* Corresponding author. *E-mail address:* f.ahmadi_uk@yahoo.com (F. Ahmadi).

the fractal analysis [32-33], geochemical indicators can be inferred for mineral potential/prospectivity mapping (MPM).

In MPM, the locations of known deposits can be used to evaluate the performance of the prepared prospectivity models. This is obtained by overlaying mineral deposit locations on a categorized exploration targeting model [34-36]. MPM is a multi-criteria decision-making task (MCDM) that aims to outline and prioritize prospective areas for guiding undiscovered mineral deposits of the type sought [35]. Bonham-Carter et al. (1989) [37], applied the weights of classes of spatial values divided by their corresponding occupied area (the area occupied by each class of evidential values) to estimate the probability of discovering mineral deposits in several classes mostly determined by fractal analysis. Yousefi and Carranza (2015, 2016) [35; 38] developed the prediction-area (P-A) plot, through which the percentage of known deposits anticipated by prospectivity classes (prediction rate) and the occupied areas of the corresponding prospectivity classes are contributed to determining the relative importance of different prospectivity models. By drawing the P-A plot, both the ore prediction rate and the occupied area of exploration targets contribute to the evaluation of prospectivity models [35; 39-44]. Thus, if two different prospectivity models delineated exploration targets with different occupied areas, but with the same prospectivity score, the performance of the prospectivity model with the smaller target areas is higher than that of the model with larger target areas [44].

Each of these evidence maps should be generated by using logistic functions before drawing the P-A plots and fractal curve [35]. Spatial evidence values in each map are transformed using a logistic function because it can be used for the proper transformation of unbounded values into a range of [0,1] [45]. Therefore, using a logistic function avoids the disadvantage of data-driven approaches to MPM in terms of exploration bias and stochastic error in delineating target areas that are generally portrayed near and around the known mineral occurrences [46].

The focus of this study is on the identification of geochemical anomalies in the Esfordi 1:100,000 geochemical data sheet using stream sediment samples. Through multi-variable analysis of geochemical data (clustering and principal component analysis "PCA") after preprocessing of all input elements, several indicators are prepared to be projected by a logistic function into an interval depicting Fe favorability. Simultaneous consideration of the C-N fractal curve and the P-A plot provide insights about the data-driven weight of each indicator map in association with Fe occurrences. Finally, a multi-class index overlay MPM is generated for further guiding of Fe targeting.

2. Geological setting of Esfordi district

Gansser(1981) has stated that Iran and the surrounding areas consist of a mosaic of continental blocks separated from each other by complex fold-and-thrust belts within the Alpine-Himalayan orogenic system [47]. The oldest basement is located in the Central Iran terrane and is composed of a Precambrian basement with a Paleozoic to Mesozoic [2]. The Bafq district of Central Iranian Microcontinent (CIM) is part of a Gondwana fragment that is situated between the Alpine Zagros and Alborz belts[48]. From east to west, this district is divided into three major crustal domains; the Lut, Tabas, and Yazd blocks [49]. The Tabas and Yazd blocks are composed of variably deformed and fault-bounded supracrustal rocks [50] and are separated by the nearly 600 km-long, 80 km-wide, arcuate, and structurally complex Kashmar–Kerman Tectonic Zone (KKTZ). The KKTZ provides remarkable exposures of the Ediacaran and mainly lower Paleozoic CIM successions. The Bafq district in the central section of the KKTZ hosts various iron oxide ores (1.8 Gt; NISCO 1980) that are distributed within 34 iron ore anomalies from Robat-Posht-Badam in the north to Bafq in the south. In the following, iron oxide ores in the Bafq district that are related to the Prototethyan Ocean, are discussed [48]. The Posht-e-Badam Block in the microcontinent of Central-East Iran is known as Iran's main metallogenic province, hosting many ores, especially iron oxide-apatite (IOA), Fe-Mn exhalative, and Zn-Pb sedimentary exhalative types [49]. The iron oxides of the Bafq district as the Kiruna-type deposits (Fig. 1) have the same age of formation as related volcanic and plutonic host rocks[4; 7; 50; 51]. The hydrothermal mineralization of Magnetite-Apatite occurs mainly as massive orebodies and metasomatic replacements with locally elevated contents of rare earth elements and peripheral uranium mineralization. Recently deposits of the Kiruna type are commonly referred to as IOA [52] or P-rich iron oxide deposits [53]. Other hosts of the P-rich iron ore in the Sechahun region are limestone and dolomite, in addition to volcanic rocks. In the eastern highlands of the Sechahun area, alternating layers of dolomite, hematite, and jaspilite exist. The mining district of Bafq lies in the center of the volcano-plutonic arc of Kashmar-Kerman, between Kuhbanan and Kuhe-Daviran, the main fault systems of Central Iran. This magmatic arch hosts important deposits of magnetite-apatite Kiruna type and extends from Robat-Posht-Badam in the north to Bafq in the south as a narrow rift zone [54]. A huge complicated of volcanogenic-sedimentary, metamorphic, and magmatic rocks participated inside the geological structure of the Sechahun location. Based totally on geological mapping and subject research, there are three complexes of Precambrian-Early Cambrian, Cambrian-Tertiary, and Quaternary rocks in the vicinity. The Precambrian formations arise chiefly in the south of the Sechahun, northeast of the Bafq. They constitute foundation protuberances composed of rhyolite, crystalline schist, gneiss, effusive green rocks, and marble. Iron and Fe-Mn deposits in the Kashmar-Kerman volcano-plutonic arc within the Bafq district evolved for the duration of successive phases. The primary section is related to the Rizu and Dezu formations (Narigan Fe-Mn deposit and layered part of Mishdovan deposit, which also have a minor Mn, REE, and U mineralization), and the second phase is associated with basic and ultrabasic intrusions, consist of the Chador-Malu, Choghart, Se-Chahun, ChahGaz, Mishdovan, Gasestan, North Anomaly and LakkehSiah deposits (Kiruna-type iron deposits) [4; 8; 11; 51].

Maximum of the Iranian iron ore reserves are located in the Bafq district in the center of Iran which were significantly explored in the course of the 1960s and 70s in an Iranian-Russian cooperation undertaking whilst 34 aeromagnetic anomalies have been delineated, of which four deposits are presently mined. Individual deposits range up to several hundred million tons of iron ore with variable amounts of apatite. The iron ore deposits of the Bafq district are associated with volcano-sedimentary rocks and high-degree intrusions and have a sulfide-poor mineral assemblage of low-Ti magnetite (±hematite) with varying however feature amounts of fluorapatite and actinolite. This assemblage is far just like the ore deposits of the Kiruna district in northern Sweden, whence such ores are named as "Kiruna-type" [13]. The Bafqmetallogenic province hosts world-class and high-grade Kiruna-type iron oxide-apatite-REE ore deposits (>2000Mt, Fe 45-65 wt%) [56], within the Ediacaran, to lower Cambrian formations [2; 4; 7; 11;54]. In addition to the mineralization of iron oxide-apatite, several non-Fe ore bodies contain Pb-Zn, P, REE, Mn, and U. The tectono-magmatic evolution and related mineralization (e.g., iron oxide-apatite-REE) in the Bafq district continue to be not fully understood [7]. According to [51; 54], this mineralization is related to intra-continental rifting and is associated with magmatic events that occurred within Gondwanaland. In contrast, Ramezani and Tucker (2003) [50], proposed that the evolution of the Bafq district was related to arc magmatism along the Prototethyan margin of Gondwana. This interpretation is based on the trace-element characteristics of the intrusive and volcanic rocks and the juxtaposition of the fragmented remains of the continental margin and cover sequences [58].

The Esfordi 1:100,000 sheet is situated in the Bafq-Posht-e-Badamzone. The oldest deposits in this area are a series of quartz sandstones and it is a silty shale with lenses made of 20 to 30 cm thick thin crystalline black limestone and several layers of black silk between them. The sediments belonging to the Upper Precambrian-Lower Cambrian with a few sandstone are located on older sediments with angular heterogeneity and consist of two lower and upper parts. The lower part includes dolomite, limestone, shale and sandstone, acid lavas, acidic expectations, calcareous shale, shale, and sandstone. The upper part is often included carbonate. These sediments are comprised of dolomite to calcareous dolomite, dolomite limestone, and thick layer limestone. The presence of an angular discontinuity under the Cambrian-Precambrian precipitates indicates that the event Pre-Cambrian mountaineering is one of the oldest reported movements in this region. These movements can be compared to the asynchronous phase. Carboniferous sediments are formed by epeirogeny. The presence of intermediate to upper premium deposits is a sign of progress the sea is back in the late Paleozoic [4; 54]. The Esfordi apatite-magnetite deposit is located 35 km northeast of the Bafq. Esfordi was initially investigated in the early 1970s for its iron ore potential but due to the presence of high-grade apatite mineralization, it has been studied for its phosphate potential by the Geological Survey of Iran since 1981. After detailed exploration (drilling of more than 70 exploration boreholes) during 10 years (1982-1992), plant construction started in 1993, and mining activity began in 1999 with the production of a phosphate concentrate for use in the fertilizer industries and phosphoric acid.

Geological descriptions of 22 iron ore occurrences within the Esfordi district have been tabulated in Table 1 and plotted over the subset geological map shown in Fig. 1

Table 1. The geological description of all Fe occurrences in the Esfordi district [51].

No	Name	Host rock/age
1	Anomaly No. X	Sandstone and shale/Paleozoic
2	Anomaly No.II B	Metamorphic and metasomatic rocks/Precambrian
3	Anomaly No.II C	Metamorphic and metasomatic rocks/Precambrian
4	Anomaly No. IV	Metamorphic and metasomatic rocks/Precambrian
5	Anomaly No. V B	Sandstone and shale/Paleozoic
6	Anomaly No. V C	Sandstone and shale/Paleozoic
7	Anomaly No.VIII	Granite, volcanic, and sandstone/Upper Precambrian
8	Anomaly No. XI	Sandstone and shale/Paleozoic
9	Anomaly XIIA	Volcano–sedimentary rocks/Precambrian–Cambrian
10	Anomaly No.XIII A	Porphyry granite/Upper Precambrian
11	Cheshmehfiruz	Acidic to intermediate volcanic and dolomite/Upper Precambrian
12	Choghart	Alkali granite, volcanic, sandstone, and schist/Upper Precambrian
13	East of Bafq	Alkali granite, acidic volcanic, dolomite, and limestone/Upper Precambrian
14	Esfordi	Alkali granite, acidic volcanic, dolomite, and limestone/Upper Precambrian
15	Lakkehsiah	Alkali granite, acidic volcanic, dolomite, and limestone/Upper Precambrian
16	Mishdovan	Alkali granite, volcanic, and sandstone/Upper Precambrian
17	Mobarakeh	Metamorphic rocks/Precambrian
18	Nargun	Alkali granite, acidic volcanic, dolomite, and limestone/Upper Precambrian
19	Narigan	Volcanics and sandstone/Upper Precambrian
20	North of Sechangi 1	Sandstone and shale/Paleozoic
21	North of Sechangi 2	Sandstone and shale/Paleozoic
22	Sechahun	Diorite, volcanosedimentary/Upper Precambrian–

3. Methodology

3.1. Geochemical data analysis

As it was mentioned before; in this study, 843 stream sediment samples were collected to be analyzed by an ICP-MS instrument for 19 elements and oxides. Preprocessing of elements concentration was performed for outlier data correction through the DORFEL method [59-60].To detection of outlier data, the mean and standard deviation of data are calculated without considering the largest amount of data. Then the largest amount of values is considered as outlier data if it satisfies the following equation:

$$X_A \geq \overline{X} + S * g \quad (1)$$

In this equation, g is the threshold of outlier values, X_A, $\overline{X}$ and S are the largest amount of values, average and standard deviation, respectively. Based on the results of this method, 10.8% for Fe_2O_3, 1.88% for TiO_2, and 699 ppm for *V* have substituted instead of outlier values.

Then, the normal or abnormal concentration distribution of these elements was evaluated, and some elements were normalized by a logarithmic operation, and the Cox-Box method was used to normalize other elements [58-60]. It helps to better find out the spatial correlation of elements in association with the sought Fe-bearing target when implementing single or multi-variable geochemical data analysis. Taking the geological and Google Earth Maps into account, the stream sediments of the Esfordi sheet were plotted in Fig. 2 by overlaying the locations of all geochemical samples. Univariate statistical analysis results indicate that Fe_2O_3, TiO2, and *V* mean values are 5.54%, 0.795%, and 84.83 ppm, respectively. The statistical summaries of these elements have been presented in Table 2. Histogram and box plots of the element concentration were portrayed in Fig. 3 to attain general insights about the characteristics of each variable in the Esfordi district. The range of values and frequency of each variable can be deduced from histogram plots. By looking at the Cox-Box plots, different quartiles and outlier data can be identified.

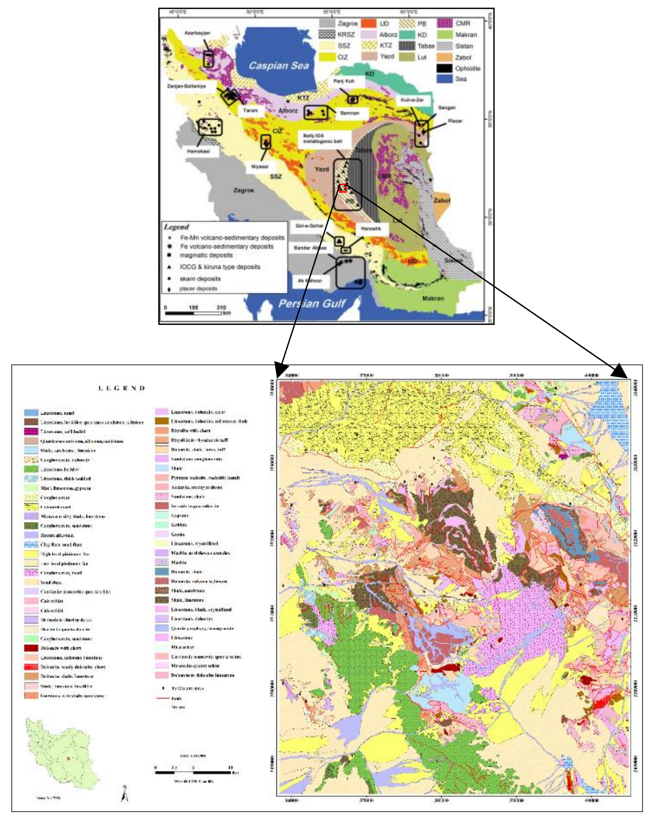

Fig. 1. Distribution of iron deposits in Iran [55] and an enlarged geology view of the Esfordi district.

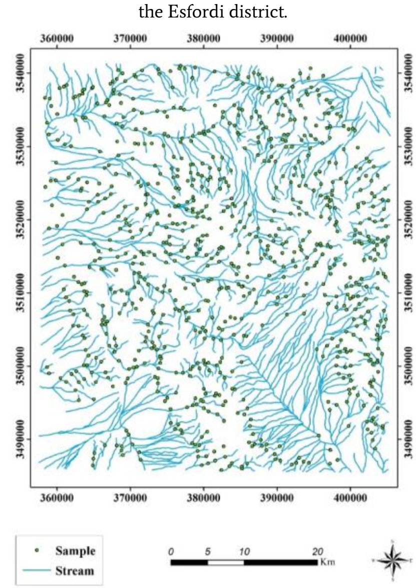

Fig. 2. Stream sediment geochemical samples over the Esfordi district.

Table 2. The statistical characteristics of geochemical concentrations.

	Number	Minimum	Maximum	Mean	Standard Deviation
Fe_2O_3 (%)	843	2.70	10.80	5.54	1.23
TiO_2(%)	843	0.01	1.88	0.795	0.167
V (ppm)	843	7.00	699	84.83	2.312
Main Factor	843	0.1	5.05	2.11	1.40

One of the methods that has been widely used in studying the geochemical model of elements is the multivariate statistical methods that can also help to classify and rank the anomaly in the geochemical data.[61]. One of the multivariate statistical methods is the correlation coefficient between the elements, which can identify the main variables associated with mineralization. The clustering method was used to investigate the correlation among the elements. The result of cluster analysis using ward's method [62-63] for 19 geochemical variables have been presented in a dendrogram plot in Fig. 4. According to this diagram, iron has the most correlation with TiO_2 andP_2O_5 than with *V*, B, and Cr. The correlation between the elements was determined using Pearson's method and listed in Table 3. According to this table, the highest correlation is between TiO2 and Fe_2O_3 equal to 0.690.

Factor Analysis is also a dimension reduction tool in statistical analysis [58; 64-65], which has attracted the attention of scholars to find out the main factor(s) from several geochemical variables. The multivariate statistical analysis, specifically factors analysis, is an appropriate technique for behavioral characteristics and reduce the number of geochemical variables. Factor analysis has been widely used for the interpretation of stream sediment geochemical data [25; 66-68]. The ultimate goal of the factor analysis is to explain the variations in a multivariate data set by a few factors as possible and to detect hidden multivariate data structures. Factor analysis is suitable for the analysis of the variability inherent in a geochemical data set with many analyzed input elements. Consequently, factor analysis is often applied as a powerful tool for exploratory data analysis [25; 58].

For reduction of variables, factor analysis was performed for the stream sediments geochemical data, where Table 4 has listed the main six factors. The main variables of each factor are determined based on the values obtained in each of the factors that are (1) Fe_2O_3, TiO_2, and *V*, (2) SiO_2, CaO and B, (3) Ni and Cu, (4) MgO, (5) Li and (6) Sr. The first factor with high loading of the Fe_2O_3, TiO_2, and *V* is used as a geochemical indicator and footprint in association with Fe-bearing regions. It is worth pointing out that the *V* element has the strongest correlation with the Iron-oxide distribution. The grade of iron in the minerals of this area is directly proportional to the grade of *V* and TiO_2, and inversely proportional to the amount of phosphorus element.

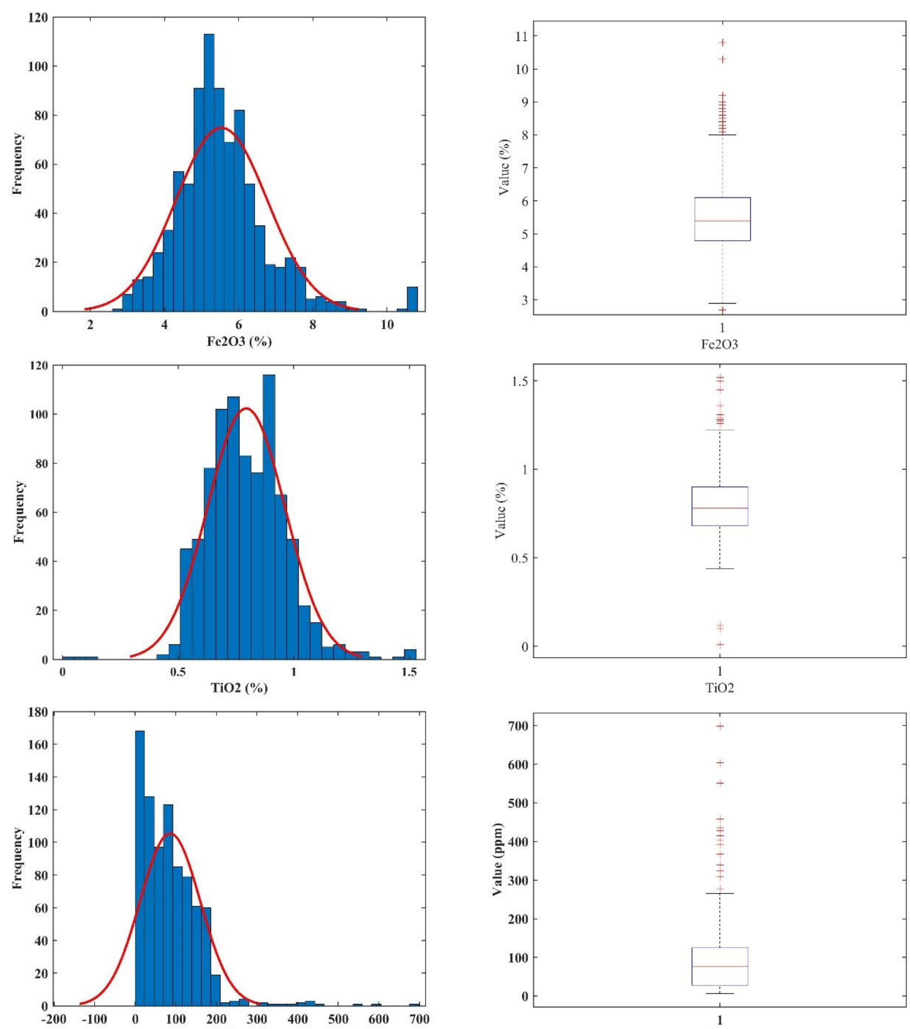

Fig.3 Statistical charts of histogram plot and box-plot for three geochemical elements of Fe_2O_3 (1st row), TiO_2(2nd row), and V (3rd row).

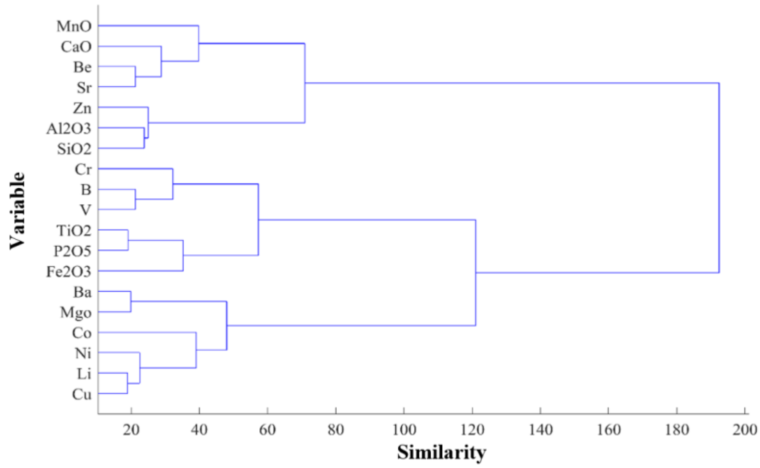

Fig.4 The result of cluster analysis for 19 geochemical elements in the Esfordi district.

Table 3. The Pearson correlation coefficients of important variables.

Fe2O3	1											
TiO_2	0.690	1										
MnO	0.408	0.329	1									
V	0.393	0.113	0.454	1								
Cr	0.380	0.247	0.037	0.052	1							
Ba	0.410	0.370	0.532	0.284	0.080	1						
SiO_2	0.318	0.272	0.164	0.290	-0.240	0.286	1					
Al_2o_3	0.301	0.197	0.156	0.174	-0.019	0.236	0.461	1				
P_2O_5	0.442	0.281	0.344	0.290	-0.075	0.345	0.160	0.269	1			
B	0.350	0.250	0.234	0.206	0.080	0.450	0.455	0.477	0.308	1		
Ni	0.283	0.292	0.039	-0.200	0.374	0.111	0.061	0.269	0.223	0.252	1	
Co	0.493	0.305	0.187	0.052	0.280	0.198	0.116	0.269	0.231	0.198	0.404	1
	Fe2O3	TiO_2	MnO	V	Cr	Ba	SiO_2	Al_2o_3	P_2O_5	B	Ni	Co

3.2. Concentration-number (C-N) fractal discretization of evidential maps

Fractal methods can illustrate the relationship between the geological, geochemical, and mineralogical information [18; 21; 33; 69]. Among several versions of fractal methods, the concentration-number (C-N) model can be adopted to explain how geochemical population is distributed without data pre-analysis [59; 70-71]. This model shows that there is a spatial relationship between the input attribute and the sample numbers. The C-N model can be defined by the following equation:

$$N(\geq \rho) = F\rho^{-D} \quad (2)$$

Where ρ is the element concentration and N(≥ρ) is the overall number of samples having concentrations equal to or higher than ρ, also "F" is a constant, and "D" is a benchmark power for fractal dimensions of concentration distribution. In addition, a curve of N(≥ ρ) versus ρ in a log-log plot indicates the linear parts with different slopes "–D", corresponding to different concentration ranges [69-70; 72].

Based on the C-N log-log plot, there are four geochemical populations for Fe_2O_3 shown in Fig. 5a, where the anomalous zone has a threshold value of 9.23%, marked in red (Fig. 5b). The result of the classification of TiO_2 is four geochemical populations depicted in Fig. 6a. According to this plot, a threshold of 1.24% separates the anomalous zone marked in red (Fig.6b). Six geochemical populations for *V* were observed in Fig. 7a, and a threshold value of 399 ppm is extracted as the border of favorable zones probably in association with Fe targeting (red regions in Fig. 7b). Based on reclassified fractal maps, High intensive anomalies of Fe_2O_3, TiO_2, and *V* commence from 10.80%, 1.88%, and 699 ppm, respectively. However, the C-N log-log plot of the main factor was plotted showing five populations (Fig. 8a) with an anomalous threshold of 4.49, marked with brown color in Fig. 8b.

Table 4. The factor analysis of 19 geochemical variables and the main six components.

	C1	C2	C3	C4	C5	C6
Fe_2O_3	**0.754**	0.170	0.224	0.173	-0.348	0.014
TiO_2	**0.613**	0.082	0.376	-0.088	-0.490	-0.026
MnO	**0.535**	-0.060	0.590	0.100	0.319	-0.193
Zn	0.337	0.622	-0.041	-0.076	0.232	-0.380
Cu	0.406	0.165	-0.582	0.247	0.182	0.323
V	**0.535**	-0.315	0.291	0.438	0.362	0.202
Sr	-0.029	0.567	0.034	0.198	0.113	-0.622
Al_2o_3	**0.650**	-0.089	-0.456	0.048	0.077	-0.092
P_2O_5	**0.558**	-0.016	0.189	-0.128	0.404	0.184
CaO	-0.554	0.651	0.054	0.119	0.113	0.258
MgO	0.134	0.365	0.305	-0.695	0.267	0.105
SiO_2	**0.562**	-0.433	-0.239	-0.147	-0.231	-0.303
Cr	0.123	0.688	0.136	0.466	-0.296	0.142
Ni	0.423	0.580	-0.095	-0.389	-0.109	0.225
Co	0.491	0.439	-0.096	0.032	-0.067	0.244
Ba	**0.590**	-0.163	0.377	0.139	0.051	0.035
B	**0.696**	-0.228	-0.213	-0.140	0.103	0.110
Li	0.301	0.170	0.224	0.173	-0.348	0.014
Be	**0.570**	0.082	0.376	-0.088	-0.490	-0.026

The reclassified fractal-based Fe_2O_3 map was divided into four classes while the lowest class lies at an interval of 2.7-4.68 % and the highest one at 9.23-10.8 % (Fig 5b). Areas of different classes from the lowest class to the highest one are marked with green, blue, yellow, and red respectively. Regions with a high probability of mineralization are shown in red color. These areas are often seen in the west, the north, and the center of the Esfordi district. TiO_2 reclassified fractal map shown in Fig. 6b, indicates four different classes, where the lowest class is at an interval of 0.02-0.64% and the highest one at 1.24-1.88 %. High mineralization probability is shown in red color. These zones are frequently seen in the west and the north of the area. The reclassified fractal *V* map shown in Fig. 7b has six classes. The lowest class includes the values of 0-55 ppm (in green color) and the highest class is at 399-699 ppm (in brown color). The anomalies in this map are shown in red and pink colors. These anomalous zones are found in the NW, the west, and pretty in the SW of the study area. Finally, the fractal reclassified map of the main factor has five classes. The lowest class was marked as green and the highest class was marked as brown (Fig. 8b).

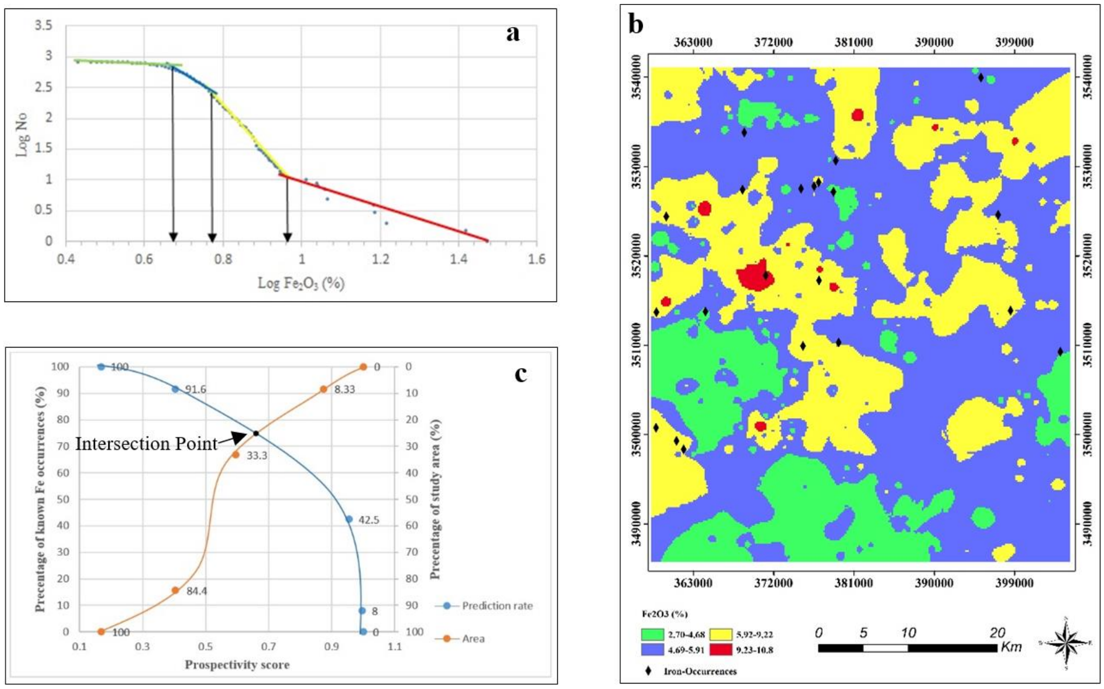

Fig.5 Geochemical distribution map of Fe_2O_3, (a) C-N log-log plot, (b) reclassified fractal-based evidential map, and (c) P-A plot.

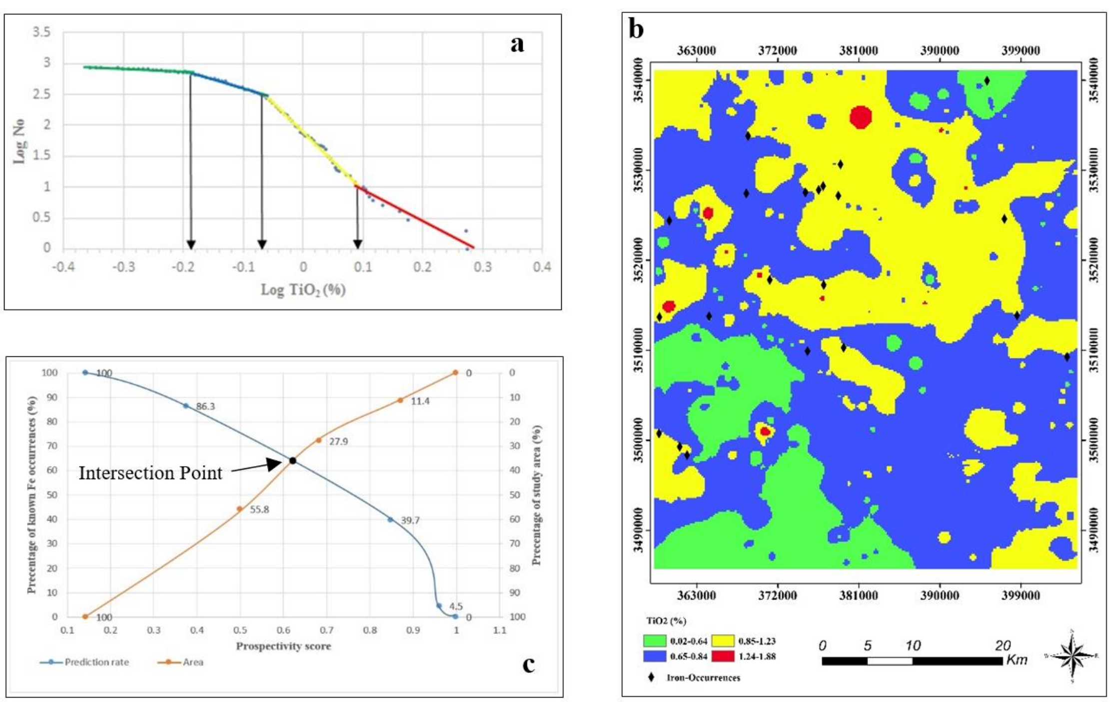

Fig.6 Geochemical distribution map of TiO_2, (a) C-N log-log plot, (b) reclassified fractal-based evidential map, and (c) P-A plot.

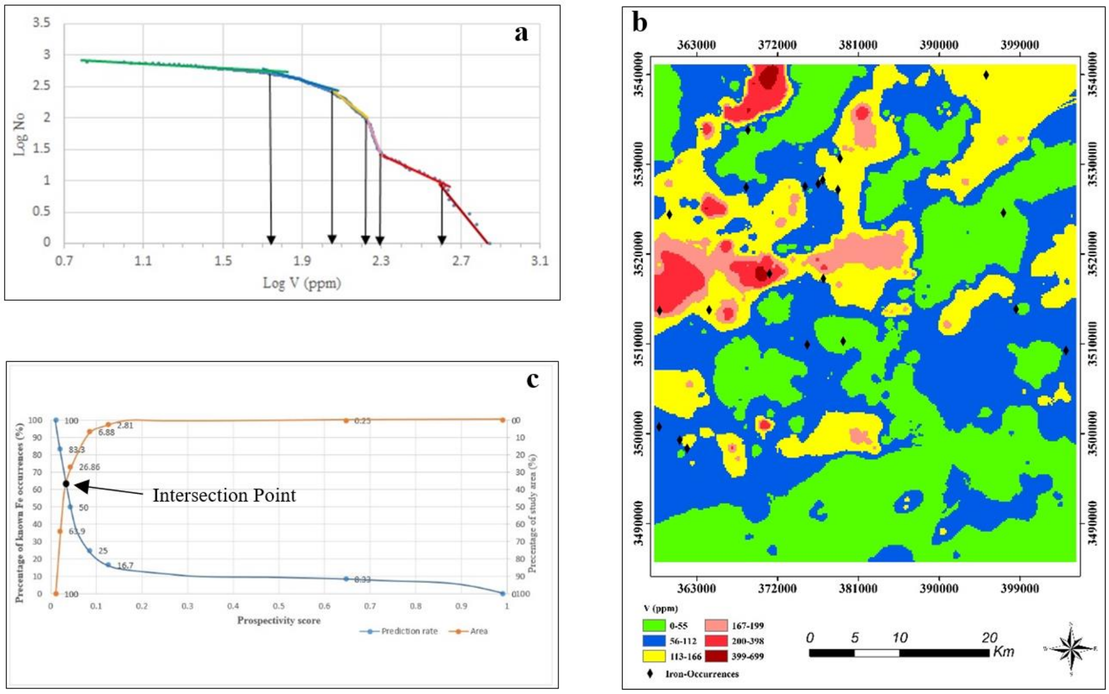

Fig.7 Geochemical distribution map of *V*,(a) C-N log-log plot, (b) reclassified fractal-based evidential map, and (c) P-A plot.

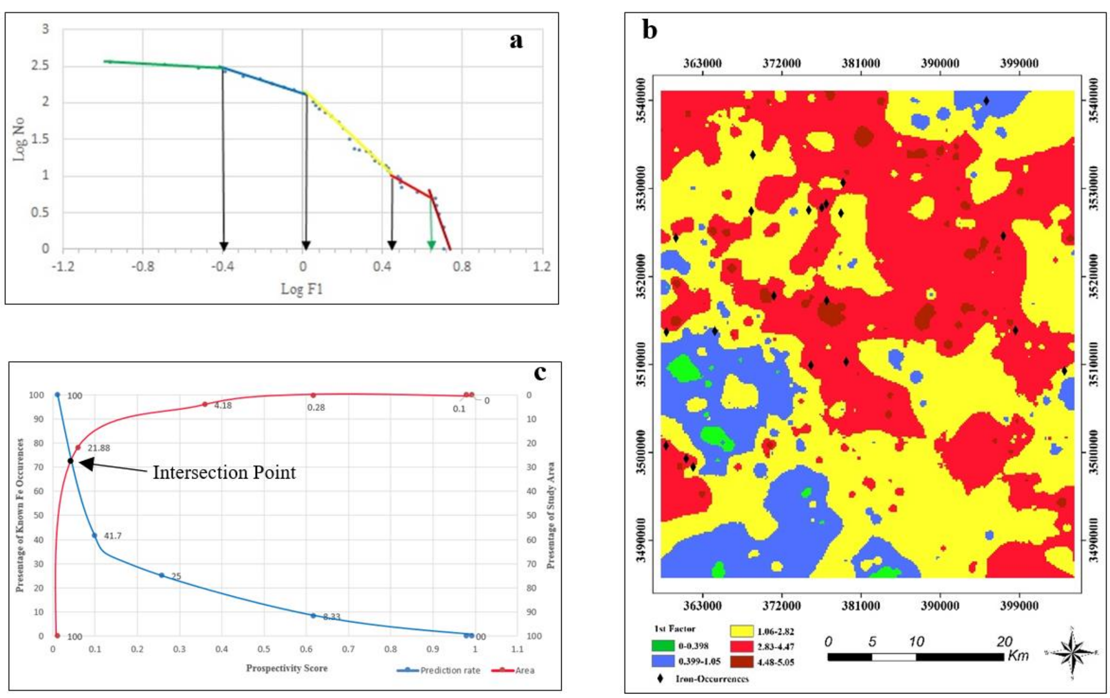

Fig.8 Geochemical distribution map of the main factor,(a) C-N log-log plot, (b) reclassified fractal-based evidential map, and (c) P-A plot.

3.3. Prediction-area (P-A) plot

The X value versus the intersection point can be used as a threshold in the P–A plot of an evidence layer to create a binary evidence map for use in Boolean logic MPM [34]. A majority of mineral deposits are connected to the range from X to the maximum evidential values [32]. In MPM, weights assigned to spatial evidence must reflect realistic spatial associations between spatial evidence and mineral deposits sought. Therefore, the locations of known Fe occurrences can be used to assist the reliability of assigned weights to spatial evidence representing their spatial associations with mineralization in the Esfordi district (Table 1). In a P-A plot of an evidence map, there are two curves, the curve of prediction rate of known mineral occurrences corresponding to the classes of the weighted evidential map and the curve of a percentage of occupied areas corresponding to the classes of the weighted evidential map. Usually, a fractal model is used to separate different populations/classes within an indicator/evidence map. In the P-A plot of a given evidence layer, if the intersection point shows a higher *Y* value in the left axis (i.e., higher prediction rate) in comparison with the P-A plot of other evidence layers, it means the former has a lower *Y* value in the right axis (i.e. smaller occupied area). Because the sum of ore prediction rate and the occupied area at the intersect point is equal to100. Thus, if the two curves intersect at a higher place of the P-A plot of an evidence layer (in comparison with other evidence layers), it represents a smaller area containing a large number of mineral deposits. It means that a higher probability of mineral deposit occurrence exists for this class within the evidence map [32].

The P-A plot of Fe_2O_3 variables shown in Fig. 5c predicts 25% of the study area as a favorable zone and 75% of the known Fe occurrences. The P-A plot of TiO_2 shown in Fig. 6c predicts 37% of the study area with an ore prediction rate of 63%. For *V* element, Fig. 7c has predicted 36% of the study area with an ore prediction rate of 64%. Note that the occupied area and ore prediction rates are 27% and 73%, respectively (Fig.8c), for the main geochemical factor. The extracted parameters at intersection points of the P-A plots for geochemical evidence are listed in Table 5.

Table 5. The extracted parameters at the intersection point of P-A plots for evidential maps.

Evidential Map	Prediction Rate (%)	Occupied Area (%)	Normalized Density	Weight
Fe2O3	75	25	3	1.099
TiO_2	63	37	1.703	0.532
V	64	36	1.780	0.577
Main Factor	73	27	2.704	0.994
MPM	78	22	3.545	1.265

3.4. Geochemical Fe prospectivity map

In this paper, the values in evidence maps are transformed using a logistic function in the range of [0,1]. Whereas the weights of individual evidence maps are assigned by the use of the P–A plot in a data-driven way [32]. Four geochemical maps of Fe_2O_3, TiO_2, *V,* and main factor were prepared based on the fractal-number method. Geochemical Fe prospectivity map through the integration of all evidential layers is shown in Fig 9b. The integrated map has six classes(Fig. 9a) that the lowest class includes the values of 0-0.121 (in green color) and the highest class is at 0.48-1 (in brown color). Based on the intersection point in Fig 9c, the geochemical Fe prospectivity map has occupied 22% of the study area as favorable zones by which 78% of the known Fe occurrences are delineated. The synthesized evidence map has more weight than other geochemical layers (Table 5), showing its superiority over each evidence. The weights were calculated through a natural logarithm of the ratio of ore prediction rate to the occupied area at an intersection point. This means that the intersection point in the P-A plot of the MPM has more value(78% >75, 73, 64, and 63%) than any indicators of the multi-class index overlay maps. On other hand, the final Fe prospectivity modeling has the highest ore prediction rate of mineral occurrences.

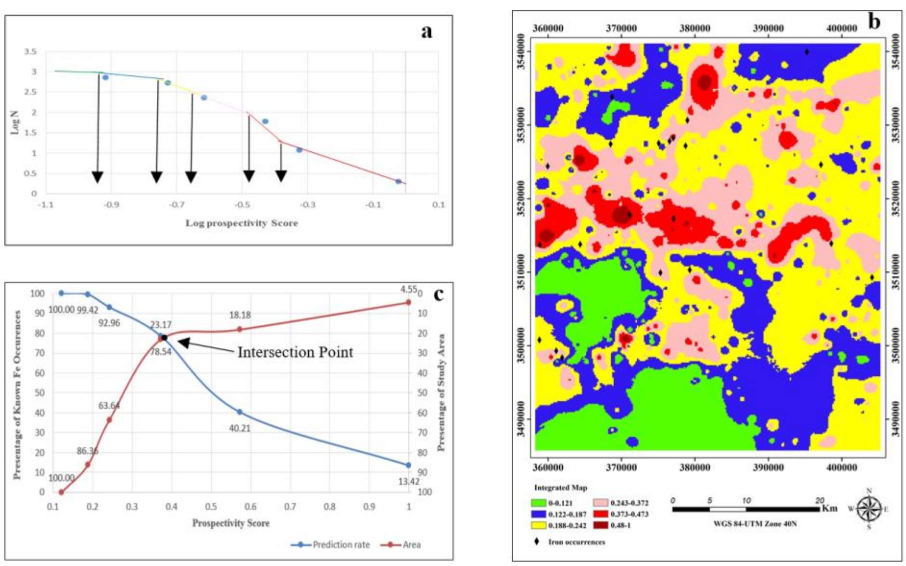

Fig.9 Multi-class index overlay geochemical prospectivity map through the integration of all evidential layers, (a) C-N log-log plot, (b) reclassified fractal-based evidential map, and (c) P-A plot.

4. Conclusion

Highly mineralized zones in the fractal models have a strong and significant relationship with favorable regions on the synthesized evidence map shown in Fig. 9b. The main anomalous regions of the Fe_2O_3, TiO_2, *V,* and main factor were located in the northern, central, and western parts of the area. The geological map shows that favorable areas are more common in rhyolite to rhyodacite, rhyolitic to rhyodacitic tuffs, colored marl, and low-level piedmont fan units. However, a high intensive anomaly of V was indicated in the NW part of the area, associated with moderate intensity of Fe_2O_3 and TiO_2 (Fig.7b). Correspondence between rock types and elemental distribution from the C-N method shows that rhyolite to rhyodacite rocks have a relationship with Fe anomalies, especially in the western and central parts of the area.

According to the results of the prospectivity layers and integrated map, some areas can be introduced as new anomalies in the region. Especially some anomalies in the NE part of the region

Another point that should be mentioned is that the synthesized evidence map with the multi-class index overlay map could depict favorable zones with higher efficiency in comparison to each evidence. Thus, this criterion can be cast in a geospatial database as a powerful footprint in Fe-bearing exploration and needs to incorporate geological and geophysical criteria to amplify the final synthesized evidence map with higher ore prediction rate and lower occupied area as favorable regions.

Acknowledgments

The authors thank the Geological Survey and Mineral Exploration of Iran for providing the data of this research.

REFERENCES

[1] Karimpour M. 1989. Applied Economic Geology. Javid Publication, Mashhad, Iran, 404 pp.

[2] Förster, H., and Jafarzadeh, A., (1994). The Bafq mining district in Central Iran - a highly mineralized Infracambrian volcanic field: Economic Geology, v. 89, p. 1697-1721.

[3] Mazaheri S. A., Andrew A. S. &Chenhall B. E. (1994). Petrological studies of Sangan iron ore deposit. Center for isotope studies, Research Report, Sydney, Australia, pp. 48-52.

[4] Daliran F (2002) Kiruna-type iron oxide-apatite ores and apatitites of the Bafq district, Iran, with an emphasis on the REE geochemistry of their apatites. In: Porter, T.M. (Ed.), Hydrothermal Iron Oxide Copper-Gold and Related Deposits: A Global Perspective, vol. 2. PGC Publishing, Adelaide, pp. 303–320.

[5] Maanijou M. (2002). Proterozoic metallogeny of Iran. In: International Symposium of Metallogeny of Precambrian Shields, p. 2.13. Kyiv, Ukraine.

[6] Daliran F., Stosch H. G. & Williams P. (2007). Multistage metasomatism and mineralization at hydrothermal Fe oxide-REE-apatite deposits and 'apatitites' of the Bafq district, central-east Iran. In: Stanely C. J. eds. Digging Deeper, pp. 1501-1504. Proceedings 9th Biennial SGA Meeting Dublin, Ireland.

[7] Daliran F, Stosch HG, Williams P, Jamali H, Dorri MB (2010) Early Cambrian iron oxide-apatite-REE (U) deposits of the Bafq District, east-central Iran. Exploring for Iron oxide copper-gold deposits: Canada and Global analogues. Geol Assoc Canada, Short Course Notes 20: 143- 155.

[8] Jami M., Dunlop A. C. & Cohen D. R. (2007). Fluid inclusion and stable isotope study of the Esfordi apatite-magnetite deposit, Central Iran. Economic Geology 102, 1111-1128.

[9] Daliran, F., (1990). The magnetite-apatite deposit of Mishdovan, East Central Iran. An alkali rhyolite hosted, "Kiruna type" occurrence in the InfracambrianBafqmetallotect (mineralogic, petrographic and geochemical study of the ores and the host rocks): Ph.D. thesis, Heidelberg, Heidelberger GeowissenschaftlicheAbhandlungen 37, 248 p.

[10] Samani B. (1993). Saghand Formation, a riftogenic unit of upper Precambrian in Central Iran. Geosciences Scientific Quarterly Journal 6, 32-45. (In Persian with English abstract).

[11] Bonyadi Z., Davidson G. J.,Mehrabi B.,Meffre S. &Ghazban F. (2011). Significance of apatite REE depletion and monazite inclusions in the brecciated Se-Chahun iron oxide-apatite deposit, Bafq district, Iran: Insights from paragenesis and geochemistry. Chemical Geology 281, 253-269.

[12] Torab F., M. Lehmann B. (2006). Iron oxide-apatite deposits of the Bafq district, Central Iran: an overview from geology to mining. World of Mining—Surface and Underground 58, 355-362.

[13] Mohammad Torab, F., (2008). Geochemistry and metallogeny of magnetite apatite deposits of the Bafq Mining District, Central Iran, Doctoral Thesis, Faculty of Energy and the Economic Sciences Clausthal University of Technology.

[14] Sadeghi, B., Khalajmasoumi, M., Afzal, P., Moarefvand, P., Yasrebi, A. B., Wetherelt, A., &Ziazarifi, A. (2013). Using ETM+ and ASTER sensors to identify iron occurrences in the Esfordi 1: 100,000 mapping sheet of Central Iran. Journal of African Earth Sciences, 85, 103-114.

[15] Samani, B.A., (1988).Metallogeny of the Precambrian in Iran: Precambrian Research, v. 39, p. 85-106.

[16] Mücke, A., Younessi, R., (1994). Magnetite-apatite deposits (Kiruna-type) along the Sanandaj-Sirjan zone and in the Bafq area, Iran, associated with ultramafic and calc-alkaline rocks and carbonatites: Mineralogy and Petrology, v. 50, p. 219-244.

[17] Harris J, Wilkinson L, Grunsky E, Heather K, Ayer J (1999). Techniques for analysis and visualization of lithogeochemical data with applications to the Swayze greenstone belt, Ontario, Journal of Geochemical Exploration 67:301-334.

[18] Cheng Q (1999). Spatial and scaling modelling for geochemical anomaly separation, Journal of Geochemical exploration 65:175-194.

[19] Cheng, Q., Agterberg, F. and Bonham-Carter, G., (1996) A spatial analysis method for geochemical anomaly separation. Journal of Geochemical Exploration, 56: 183-195.

[20] Ghavami-Riabi, R., Seyedrahimi-Niaraq, M., Khalokakaie, R. and Hazareh, M., (2010) U-spatial statistic data modeled on a probability diagram for investigation of mineralization phases and exploration of shear zone gold deposits. Journal of Geochemical Exploration, 104: 27-33.

[21] Darabi-Golestan, F., Ghavami-Riabi, R., Khalokakaie, R., Asadi-Haroni, H., Seyedrahimi-Niaraq, M., 2013, Interpretation of lithogeochemical and geophysical data to identify the buried mineralized area in Cu-Au porphyry of Dalli-Northern Hill. Arabian Journal of Geosciences, 6:4499-4509.

[22] Seyedrahimi-Niaraq, M., Hekmatnejad, A., (2020). The efficiency and accuracy of probability diagram, spatial statistic and fractal methods in the identification of shear zone gold mineralization: a case study of the Saqqez gold ore district, NW Iran. ActaGeochimica, https://doi.org/10.1007/s11631-020-00413-7.

[23] Qiuming C (2000).Multifractal theory and geochemical element distribution pattern, Earth Science-Journal of China University of Geosciences 25:311-318.

[24] Hawkes RAW, Webb HE (1979). Geochemistry in mineral exploration,2nd edn. Academic Press, New York, 657 pp.

[25] Li, C.J., Ma, T.H., Shi, J.F., (2003). Application of a fractal method relating concentration and distances for separation of geochemical anomalies from background. J GeochemExplor 77: 167–175.

[26] Mandelbrot, B.B., (1983). The Fractal Geometry of Nature. WH Freeman, San Francisco, pp 1-468.

[27] Cheng, Q., Agterberg, F.P., Ballantyne, S.B., (1994). The separation of geochemical anomalies from background by fractal methods. J GeochemExplor 51: 109–130.

[28] Afzal, P., FadakarAlghalandis, Y., Khakzad, A., Moarefvand, P., RashidnejadOmran, N., (2011). Delineation of mineralization zones in porphyry Cu deposits by fractal concentration–volume modeling. J GeochemExplor 108: 220–232.

[29] Afzal, P., DadashzadehAhari, H., RashidnejadOmran, N., Aliyari, F., (2013). Delineation of gold mineralized zones using concentration-volume fractal model in Qolqoleh gold deposit, NW Iran. Ore Geology Reviews 55: 125-133.

[30] Delavar, S.T., Afzal, P., Borg, G., Rasa, I., Lotfi, M., RashidnejadOmran, N., (2012). Delineation of mineralization zones using concentration-volume fractal method in Pb-Zn carbonate hosted deposits. J. Geochem. Explor. 118, 98–110.

[31] Zuo, R., (2011). Decomposing of mixed pattern of arsenic using fractal model in Gangdese belt, Tibet, China. Appl. Geochem. 26, S271–S273.

[32] Zuo, R., Wang, J., (2016). Fractal/multifractal modeling of geochemical data: a review. J. Geochem. Explor. 164, 33–41.

[33] Panahi, A., Cheng, Q., & Bonham-Carter, G. F. (2004). Modelling lake sediment geochemical distribution using principal

component, indicator kriging, and multifractal power-spectrum analysis: a case study from Gowganda, Ontario. Geochemistry: Exploration, Environment, Analysis, 4(1), 59-70.

[34] Mirzaie, M., Afzal, P., Adib, A., Rahimi, E., &Mohammadi, G. (2020). Detection of zones based on ore and gangue using fractal and multivariate analysis in ChahGaz iron ore deposit, Central Iran. Journal of Mining and Environment, 11(2), 453-466.

[35] Nyka¨nen, V., Lahti, I., Niiranen, T., &Korhonen, K. (2015). Receiver operating characteristics (ROC) as validation tool for prospectivity models—a magmatic Ni–Cu case study from the Central Lapland Greenstone Belt, Northern Finland. Ore Geology Reviews, 71, 853–860.

[36] Yousefi, M., & Carranza, E. J. M. (2015). Prediction–area (P–A) plot and C–A fractal analysis to classify and evaluate evidential maps for mineral prospectivity modeling. Computers & Geosciences, 79, 69-81.

[37] Carranza, E. J. M., &Laborte, A. G. (2016). Data-driven predictive modeling of mineral prospectivity using random forests: A case study in Catanduanes Island (Philippines). Natural Resources Research, 25, 35–50.

[38] Bonham-Carter, G. F., Agterberg, F. P., & Wright, D. F. (1989). Weights of evidence modelling: A new approach to mapping mineral potential. Statistical Applications in the Earth Sciences, 89, 171–183.nces, 85, 103-114.

[39] Yousefi, M., & Carranza, E. J. M. (2016). Data-driven index overlay and Boolean logic mineral prospectivity modeling in greenfields exploration. Natural Resources Research, 25, 3–18.

[40] Du, X., Zhou, K., Cui, Y., Wang, J., Zhang, N., & Sun, W. (2016). Application of fuzzy Analytical Hierarchy Process (AHP) and Prediction-Area (P-A) plot for mineral prospectivity mapping: A case study from the Dananhumetallogenic belt, Xinjiang, NW China. Arabian Journal of Geosciences, 9, 298.

[41] Gao, Y., Zhang, Z., Xiong, Y., &Zuo, R. (2016). Mapping mineral prospectivity for Cu polymetallic mineralization in southwest Fujian Province, China. Ore Geology Reviews, 75: 16–28.

[42] Nezhad, S. G., Mokhtari, A. R., &Rodsari, P. R. (2017). The true sample catchment basin approach in the analysis of stream sediment geochemical data. Ore Geology Reviews, 83, 127–134.

[43] Zhang, N., Zhou, K., & Du, X. (2017). Application of fuzzy logic and fuzzy AHP to mineral prospectivity mapping of porphyry and hydrothermal vein copper deposits in the Dananhu-Tousuquan island arc, Xinjiang, NW China. Journal of African Earth Sciences, 128, 84–96.

[44] Almasi, A., Yousefi, M., & Carranza, E. J. M. (2017). Prospectivityanalysis of orogenic gold deposits in Saqez-Sardasht Goldfield, Zagros Orogen, Iran. Ore Geology Reviews, 91, 1066–1080.

[45] Roshanravan, B., Aghajani, H., Yousefi, M., &Kreuzer, O. (2019). An improved prediction-area plot for prospectivity analysis of mineral deposits. Natural Resources Research, 28(3), 1089-1105.

[46] Bishop, C. M. (2006). Pattern recognition and machine learning. springer.

[47] Coolbaugh, M.F., Raines, G.L., Zehner, R.E., (2007).Assessment of exploration bias in data-driven predictive models and the estimation of undiscovered resources. Nat. Resourc.Res.16, 199–207.

[48] Gansser A. (1981). The Geodynamic History of the Himalaya, in Zagros, Hindu Kush. In: Gupta H. K. & Delany F. M. eds. Himalaya-Geodynamik Evolution, Geodynamik Series, 3, pp. 111-121. American Geophysical Union, Washington DC.

[49] Stocklin J. (1971). Stratigraphic Lexicon of Iran; Part 1: Tehran, Geological Survey of Iran, 338 p. Tehran Iran.

[50] Alavi M. (1991). Sedimentary and structural characteristics of the Paleo-Tethys remnants in northeastern Iran. Geological Society of America Bulletin 103, 983-992.

[51] Daliran F, Stosch HG, Williams PJ (2009). A review of the Early Cambrian magmatic and metasomatic events and their bearing on the genesis of the Fe oxide-REE-apatite deposits (IOA) of the Bafq district, Iran. In: Williams P (Ed.): Smart Science for Exploration and Mining. 10th SGA Biennial, Townsville, 623–625.

[52] Gandhi SS (2003). An overview of the Fe oxide–Cu–Au deposits and related deposit types. CIM Montréal 2003 Mining Industry Conference and Exhibition, Canadian Institute of Mining, Technical Paper, CD-ROM.

[53] Williams PJ (2010). Classifying IOCG deposits. In: Corriveau L, Mumin H (Eds) Exploring for iron-oxide copper-gold deposits: Canada and Global Analogues: *Geological Association.* Canada short course notes 20: 11–19.

[54] Groves DI, Bierlein FP, Meinert LD, Hitzman MW (2010). Iron oxide copper-gold (IOCG) deposits through earth history: implications for origin, lithospheric setting, and distinction from other epigenetic iron oxide deposits. *Economic Geology* 105: 641-654.

[55] Ghorbani, M. (2013). Economic geology of Iran (Vol. 581). Berlin: Springer.

[56] Stosch HG, Romer RL, Daliran F, Rhede D (2011). Uranium-lead ages of apatite from iron oxide ores of the Bafq District, East-Central Iran. *Miner Deposita*46: 9–21.

[57] Nisco-National Iranian Steel Company (1980). Report on results of search and evaluation works at magnetic anomalies of the Bafq iron ore region during 1976-1979. Unpublished Report, p 260.

[58] Berberian M., & King G. C. P. (1981). Towards the Paleogeography and tectonic evolution of Iran. Canadian Journal of Earth Sciences 18, 210-265.

[59] Nabatian, G., Rastad, E., Neubauer, F., Honarmand, M., &Ghaderi, M. (2015). Iron and Fe–Mnmineralisation in Iran: implications for Tethyanmetallogeny. Australian Journal of Earth Sciences, 62(2), 211-241.

[60] Olea, R. A. (2006). A six-step practical approach to semivariogram modeling. Stochastic Environmental Research and Risk Assessment, 20(5), 307-318.

[61] Tahernejad, M. M., KhaloKakaei, R., &Ataei, M. (2018). Analyzing the effect of ore grade uncertainty in open pit mine planning; A case study of Rezvan iron mine, Iran. International Journal of Mining and Geo-Engineering, 52(1), 53-60.

[62] Riemann, C., Filzmoser, P., & Garrett, R. G. (2002). Factor analysis applied to regional geochemical data: problems and possibilities. Applied Geochemistry, 17(3), 185-206.

[63] Nazarpour, A., Omran, N. R., &Paydar, G. R. (2015). Application of multifractal models to identify geochemical anomalies in Zarshuran Au deposit, NW Iran. Arabian Journal of Geosciences, 8(2), 877-889.

[64] Khalifani, F., Bahroudi, A., Barak, S., &Abedi, M. (2019). An integrated Fuzzy AHP-VIKOR method for gold potential mapping in Saqez prospecting zone, Iran. Earth Observation and Geomatics Engineering, 3(1), 21-33.

[65] Grant, A. (1990). Multivariate statistical analyses of sediment geochemistry. Marine Pollution Bulletin, 21(6), 297-299.

[66] Zumlot, A. B. T. (2012). Multivariate statistical approach to geochemical methods in water quality factor identification; application to the shallow aquifer system of the Yarmouk Basin of north Jordan. *Research Journal of Environmental and Earth Sciences*, *4*(7), 756-768.

[67] Ammar, F. H., Chkir, N., Zouari, K., Hamelin, B., Deschamps, P., &Aigoun, A. (2014). Hydro-geochemical processes in the Complexe Terminal aquifer of southern Tunisia: An integrated investigation based on geochemical and multivariate statistical methods. Journal of African Earth Sciences, 100, 81-95.

[68] Karar, K., Gupta, A. K., Kumar, A., & Biswas, A. K. (2006). Characterization and identification of the sources of chromium, zinc, lead, cadmium, nickel, manganese, and iron in PM 10 particulates at the two sites of Kolkata, India. Environmental Monitoring and Assessment, 120(1-3), 347-360.

[69] Sprovieri, R., Thunell, R., & Howe, M. (2020). Paleontological and geochemical analysis of three laminated sedimentary units of late Pliocene-early Pleistocene age from the Monte San Nicola section in Sicily. RivistaItaliana di Paleontologia e Stratigrafia, 92(3).

[70] Hirst, D. M. (1974). Geochemistry of Sediments from Eleven Black Sea Cores: Geochemistry.

[71] Malinowski, E. R., &Howery, D. G. (1980). Factor analysis in chemistry (p. 10). New York: Wiley.

[72] Wu, R., Chen, J., Zhao, J., Chen, J., & Chen, S. (2020). Identifying Geochemical Anomalies Associated with Gold Mineralization Using Factor Analysis and Spectrum–Area Multifractal Model in Laowan District, Qinling-DabieMetallogenic Belt, Central China. Minerals, 10(3), 229.

[73] Goncalves MA, Vairinho M, Oliveira V (1998). Study of geochemical anomalies in Mombeja area using a multifractal methodology and geostatistics. In: Buccianti A, Nardi G, Potenza R (eds) IV IAMG'98. De Frede, Ischia Island, Italy, pp 590–595.

[74] Afzal, P., Zia Zarifi, A., &Sadeghi, B. (2013). Separation of Geochemical Anomalies Using Factor Analysis and Concentration-Number (CN) Fractal Modeling Based on Stream Sediments Data in Esfordi 1: 100000 Sheet, Central Iran. Iranian Journal of Earth Sciences, 5(2), 100-110.

[75] Momeni, S., Shahrokhi, S. V., Afzal, P., Sadeghi, B., Farhadinejad, T., &Nikzad, M. R. (2016). Delineation of the Cr mineralization based on the stream sediment data utilizing fractal modeling and factor analysis in the Khoy 1: 100,000 sheet, NW Iran. MadenTetkikveAramaDergisi, (152), 143-151.

[76] Asfahani, J. (2017). Fractal theory modeling for interpreting nuclear and electrical well logging data and establishing lithological cross-section in basaltic environment (case study from southern Syria). Applied Radiation and Isotopes, 123, 26-31.